Article:
Weng, H.-C., Rarity, J.G., Balram, K.C. et al. (2026) Photonic-integrated quantum sensor array for microscale magnetic localisation. Nature Communications, 17. 6185. ISSN: 2041-1723

https://doi.org/10.1038/s41467-026-73701-0 nature communications

Article

https://doi.org/10.1038/s41467-026-73701-0

Photonic-integrated quantum sensor array for microscale magnetic localisation

Received: 14 November 2025

Accepted: 12 May 2026

Published online: 28 May 2026

Check for updates

Hao-Cheng Weng[1], John G. Rarity[1], Krishna C. Balram[1] & Joe A. Smith[1,2]

Nitrogen-vacancy centres (NVs) are promising solid-state nanoscale quantum sensors for applications ranging from material science to biotechnology. Using multiple sensors simultaneously offers advantages for probing spatiotemporal correlations of fluctuating fields or the dynamics of point defects. In this work, by integrating NVs with foundry silicon-nitride photonic integrated circuits, we realise the scalable operation of eight localised NV-ensemble sensors in an array, with simultaneous, distinct readout of the individual sensors. Using the eight NV sensors and machine-learning methods for multi-point magnetic field reconstruction, we demonstrate microscale magnetic localisation of a 30 μm-sized needle tip. Experimentally, the needle tip can be localised with an error below its dimension and tracked dynamically with high fidelity. We use simulations of microrobot-relevant magnetic profiles as an application-motivated case study to quantify the operating bounds and requirements for translation and rotation tracking. By moving multi-NV localisation from bulk-optical addressing to a fibre-addressed, guided-wave, multi-channel architecture with simultaneous distinct readout, this work provides a scalable architecture towards magnetic localisation in optically inaccessible environments.

The spin systems of nitrogen-vacancy centres in diamond (NVs) are nanoscale quantum sensors that are optically controllable, biologically compatible, and operable at room temperature. Quantum sensing with NVs has shown impact in material science through condensed matter studies[1,2] and biomedical applications through bioimaging and subcellular sensing[3,4]. As opposed to using a single NV sensor probe, multi-NV protocols based on spatially separated single-NV or NV-ensemble sensors have shown promising advantages in resolving target dynamics in both space and time. Some recent demonstrations include the direct imaging of magnetotactic bacteria[5] and nuclear magnetic resonance (NMR) signals[6], the localisation and monitoring of point defect dynamics in materials[7,8], and the extraction of co-varying electromagnetic fluctuations and spatiotemporal correlations[9,10].

To realise multi-NV quantum sensing efficiently requires parallelism in experimental hardware for distinct control and readout of each sensor. To scale beyond dual-path confocal microscopy[9], recent efforts improve conventional widefield spectroscopy by incorporating spatial light modulators (SLMs)[11,12]. However, widefield ODMR with EMCCD cameras is constrained by frame rates with integration time ≥10 ms, which is much slower than the NV spin readout time (300 ns). To improve signal-to-noise, spin-to-charge conversion is often used, providing higher contrast at the cost of additional complexity and longer readout time (≈ 8 ms). One can also resolve individual NV sensors by utilising additional degrees of freedom, such as differences in optical resonance[7,13] or orientations[10,14]. However, this poses stringent conditions, such as low-temperature operations or strongly-biased fields, that limit scalability.

Compared to the bulk-optical methods for multi-NV addressing, photonic-integrated NV platforms uniquely enable scalable, robust, and low-crosstalk operation. Single-mode waveguides and fibre arrays

[1]Quantum Engineering Technology Labs, H. H. Wills Physics Laboratory and Department of Electrical and Electronic Engineering, University of Bristol, Bristol, United Kingdom. [2]School of Electrical and Electronic Engineering, University of Sheffield, Sheffield, United Kingdom.
e-mail: haocheng.weng@bristol.ac.uk; joe.a.smith@sheffield.ac.uk

provide per-sensor optical I/O and routing, suppressing stray fluorescence and improving channel isolation; edge-coupled photonic integrated circuits (PICs) support compact packaging with mechanically stable alignment, which we find remains stable for weeks (see Methods). Crucially, PIC multi-channel read out through single-photon detectors would avoid camera frame-rate bottlenecks in widefield spectroscopy and confocal scan overheads, allowing sub-nanosecond resolution, and is inherently compatible with time-multiplexed readout[12] towards high-density sensor grids. Existing integrated diamond platforms have largely focused on the manufacturing challenges of coupling emitters to waveguides, such as via heterogeneous integration[15]. However, the realisation of a practical quantum sensor requires more than just integration; it demands a scalable architecture for information extraction, routing excitation and collection light to multiple sites simultaneously with minimal crosstalk and uniform efficiency.

In this work, we present an operational eight-channel sensor array that bridges the gap between device physics and system-level applications. By performing Continuous-Wave Optically-Detected-Magnetic-Resonance (CW ODMR) measurements, the eight sensors record spatially-resolved magnetic fields simultaneously, allowing multi-point field reconstruction with continuous-time signal processing and direct application in magnetic localisation. We show that this readout, when combined with a neural-network reconstruction algorithm, solves the inverse localisation problem for dynamic magnetic targets, a capability inaccessible to single-sensor devices. Specifically, we estimate the static position of a 30-μm magnetised needle tip (with an error below the tip dimension) and dynamically track the tip movement to reconstruct its trajectory at minute-level frame rates. As an application-motivated case study, we simulate microrobot-relevant magnetic profiles[16] to quantify the requirements under which translation and rotation tracking become feasible, noting that rotation tracking requires vector information available in the single-NV (or oriented-ensemble) regime. In simulation with single NV sensors, both can be estimated precisely, with an average error of 10 μm and 5°. More broadly, this architecture addresses the interconnect bottleneck for scaling multi-NV protocols beyond the optical table by shifting multiplexing from bulk optics to guided-wave routing and detector-channel readout, enabling deployable localisation in optically inaccessible environments such as in vivo[17] or microfluidic[18] scenarios.

Results

Scalable NV quantum sensing with photonic integrated circuits

To operate multiple NV quantum sensors at the same time, parallel photonic channels for each sensor are required, for efficient pumping (typically 532 nm or 515 nm laser) to polarise the spins and broadband (from 600 nm to 800 nm) photoluminescence (PL) collection to distinctly read out the spins. We propose a scalable NV sensor control scheme with photonic integrated circuits and parallel fibre arrays, as shown in Fig. 1a. NV centres in nanodiamonds allow deterministic positioning of the sensors on the silicon nitride photonic waveguides. The NV centres are pumped from the top by a 515 nm laser through an 8-channel single-mode-fibre array. The PL signal is evanescently coupled to the single transverse electric (TE)-mode waveguides[15] and sent off-chip to a second 8-channel collection fibre array through edge couplers. The setup schematic is shown in Fig. 1b. Note that by coupling the NV dipole emission to single-mode waveguides, this helps reject fluorescence from the excitation fibre (up to -70 dB as shown in ref. 15) and presents superior NV-emission collection efficiency compared to multimode-fibre end-scope architectures[19].

We realise this architecture with a commercial silicon-nitride photonic chip (see Methods), consisting of sixteen parallel waveguides as shown in Fig. 1c. The central parts of the waveguides have the top silica cladding removed and sites labelled with alignment markers, allowing NV centres in nanodiamonds to be heterogeneously combined[15]. In Fig. 1d, we show the deterministic positioning of 100-nm-sized fluorescent nanodiamonds (FND) in an array through a lithographic deposition method[15,20,21] (see also Methods). The FNDs, each hosting more than 1000 NVs, are selected to guarantee near-unity NV yield per nanodiamond site and provide a strong optical signal. We show the repeatability of the method in Supplementary Section A. Note that each spot contains a cluster of FNDs in a 4 μm by 0.5 μm area (Fig. 1e), chosen to match the mode field diameter of the excitation fibre. The yellow box in Fig. 1d shows the eight NV sensors used for this work. For edge coupling, the waveguides are tapered from 500 nm to 150 nm in 140 μm at the end for mode matching (see Fig. 1f). With broadband operability, we measure a nine-fold enhancement in coupling efficiency over the NV spectrum compared to previous works with grating couplers[15] (see Fig. 1g). The in-plane coupling also presents an advantage over grating couplers for packaging stability.

In Fig. 1h, we show the experimental setup (see also Methods), where a microwave signal is delivered through a Printed Circuit Board (PCB) antenna (underneath the chip) to drive the NV spins in the array collectively. The PL signal from the eight collection fibre channels is sent to optical filtering and single photon avalanche diodes (SPADs) for detection. Note that by replacing the 8-channel excitation fibre array with an eight-by-eight matrix fibre array, the full two-dimensional NV array could be used for sensing at the same time (i.e., for the same interrogation time) with spin readout multiplexed in time[12] (details can be found in Supplementary Section J). Also, the setup generally applies to NV sensors based on single NVs or NV ensembles (see Supplementary Section G for more details).

Parallel operation of eight NV magnetic sensors

Parallel operation of the eight NV sensors is achieved only when the excitation fibre is aligned to the NV array, and all eight collection fibres are well coupled to the waveguide channels. Through scanning of the excitation fibre array while recording the PL signal from each waveguide, we show in Fig. 2a that the NV Gaussian spots are aligned within the fibre mode field diameter. Note that the waveguide-to-fibre coupling remains at up to 85% of its original efficiency (as shown in Fig. 1g) with eight channels coupled in parallel. While the spot sizes are limited by the fibre mode field diameter and the distance between the excitation fibre and the chip (which is kept within a few μm), the physical size of the sensor volume (interaction region) is defined by the deposition area (which is 4 μm by 500 nm). The brightness of each spot varies due to differences in the number of nanodiamonds on each spot, with a minimum of 200 k counts per second.

We perform CW ODMR measurements of the eight sensors at the same time. With no external field (Fig. 2b), the ODMRs show resonances (fitted to Gaussian dips) with full width at half maximum (FWHM) ≤25 MHz and contrasts ($C = (I_{\mathrm{off}} - I_{\mathrm{on}})/I_{\mathrm{off}}$ where $I_{\mathrm{off,on}}$ are PL intensities off/on resonance) ≈4% under a 31 dBm microwave driving power delivered at the source (the uniformity of the sensor spin resonance profile is supported by the results in Supplemental Section B). As each sensor is composed of clusters of randomly oriented nanodiamonds, the sensor effectively becomes a magnetic field magnitude sensor[22]. An example set of CW ODMR measurements under an external field is shown in Fig. 2c. With the ensemble effect, our sensors are more sensitive in the low-field regime due to decreased ODMR contrast and increased resonance linewidth under a larger field. This matches the simulations in Fig. 2d (see details in Methods) and previously reported results[22].

We characterise the operation of the magnetic magnitude sensors. For a DC magnetic field in the range 0.8 mT ≤ $|B|$ ≤ 1.6 mT, we show that the Zeeman splitting is proportional to the field magnitude, Fig. 2e. The solid lines present a linear fit of the data points. The external magnetic field is generated by a strong neodymium magnet 20 centimetres away (pointing along the

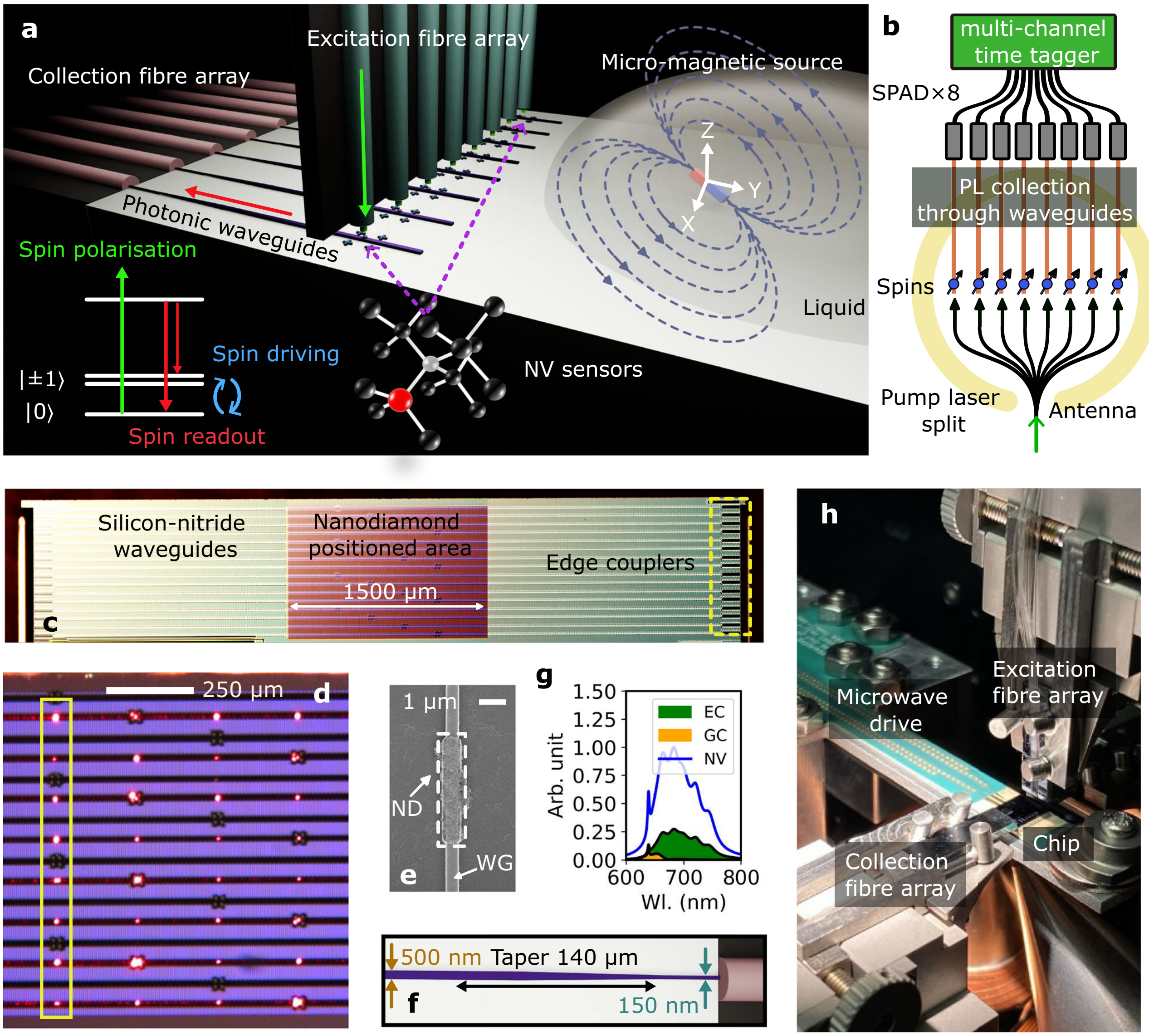

Fig. 1 | Multi-NV quantum sensing platform using photonic integrated circuits (PICs). a Schematic representation of multi-NV quantum sensing using PICs. NVs on the photonic waveguides are pumped through the top excitation fibre array and distinctly read out with PL coupled off-chip through the collection fibre array. Eight sensors are used collectively to magnetically localise the position of a microscale magnetic source. Using high-index-contrast photonic channels, magnetic localisation remains feasible when direct top-down visibility is limited (for example, obscured by a liquid). **b** Schematic diagram of the experimental setup. Eight NV-spin sensors are pumped by a 515 nm laser split into eight channels. The distinct PL signal is collected by parallel single-mode waveguides and sent to single-photon avalanche diodes (SPADs) for detection. The eight SPAD signals are sent to a multi-channel time tagger for spin-state measurements. The NV spins are driven by a global microwave antenna (yellow ring in the diagram). **c** The silicon-nitride photonic chip. Experimentally, we use only eight out of the sixteen waveguides. The middle red-shaded area is unclad for nanodiamond positioning and is in the middle of the chip for ease of operation. The edge couplers (enclosed by the yellow dashed-line box) are fabricated with a deep etch to ensure surface smoothness. **d** Image of a nanodiamond array. The nanodiamonds are visualised by scattered light when a red laser is coupled into the waveguides. Spots look extended due to the scattering of light around the alignment markers. **e** A scanning-electron-microscopic image of a lithographically-positioned nanodiamond site, showing a cluster of nanodiamonds in the rectangular window. **f** A schematic diagram of waveguide tapering to the edge couplers. The 150 nm end size is limited by the foundry's minimum feature size. **g** Comparison of the coupling efficiencies over the spectrum for edge couplers (EC) and grating couplers (GC). The normalised NV spectrum (blue, simulated following ref. 52) is compared to those multiplied by the waveguide-to-fibre efficiencies for EC (green) and GC (yellow). Wavelength abbreviated Wl. **h** Experimental setup, showing the excitation and collection fibre array, the chip, and the PCB microwave antenna.

waveguide direction) to ensure field homogeneity across the eight sensors. The field range measured is only a subset of the full operation range and is selected for experimental convenience. The average slope is 22 ± 3 MHz/mT due to the averaged response of isotropic NV orientations (see derivation in Methods and similar simulation results in Supplementary Section C). The reduced effective gyromagnetic ratio for NV ensembles in FND is similarly observed in ref. 22,23. The magnetic field sensors are characterised by the CW ODMR sensitivity (units: T/$\sqrt{\text{Hz}}$)[24]

$$\eta_{\text{cw-ODMR}} = \frac{4}{3\sqrt{3}}\frac{h}{g_e\mu_B}\frac{\Delta\nu}{C_{\text{cw}}\sqrt{R}}, \tag{1}$$

where h is the Planck constant, g_e the electron g-factor, μ_B is the Bohr magneton, $\Delta\nu$ is the resonance linewidth (FWHM), C_{cw} is the CW-ODMR contrast, and R is the photon-detection count rate. The η_{cw}

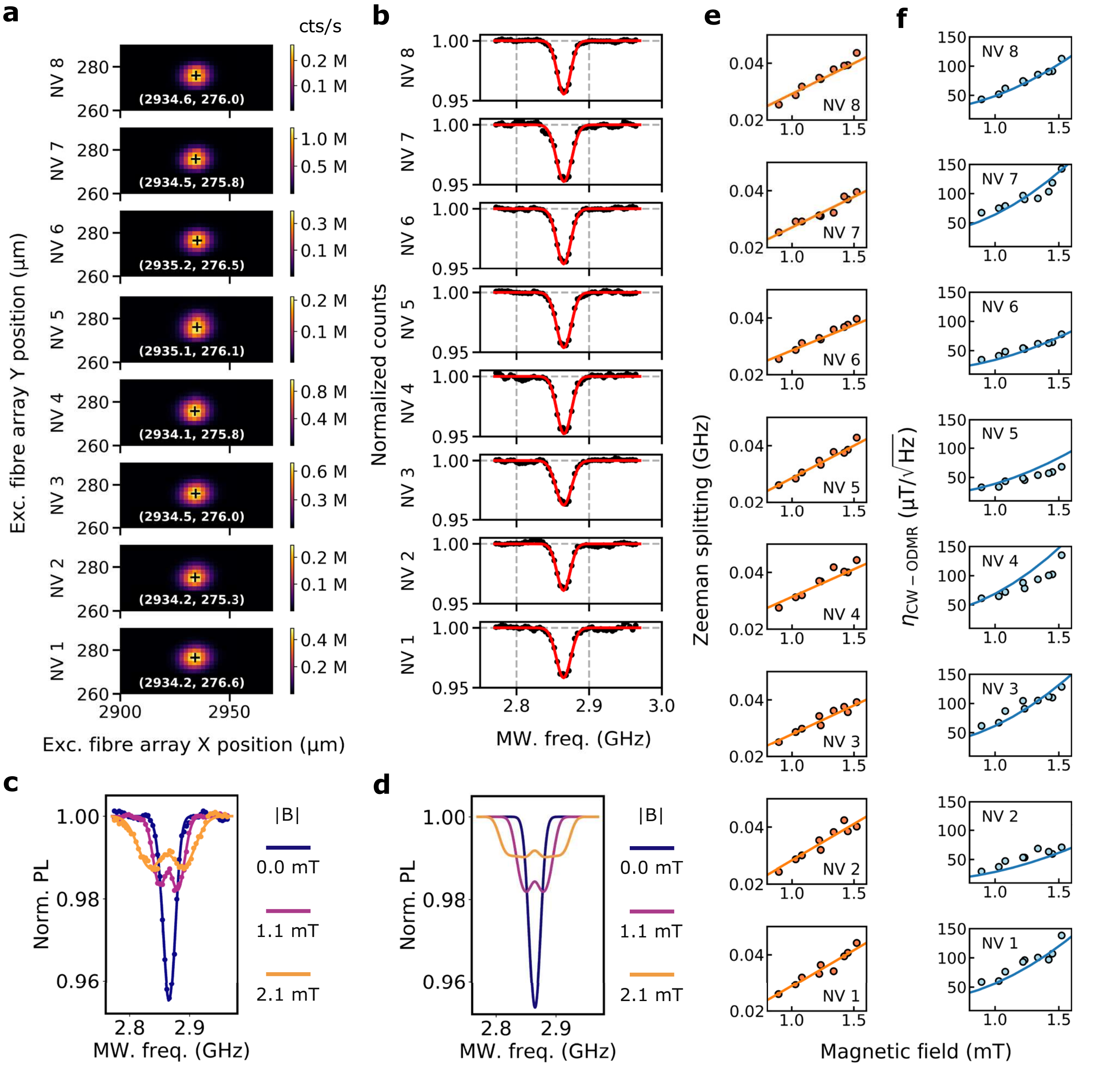

Fig. 2 | Parallel sensor operation and characterisation. **a** The PL signal of the eight NV-ensemble sensors collected from each waveguide when the excitation (exc.) fibre array is scanned. Here, the X direction is parallel to the waveguides. Fitted centres of the Gaussian spots are labelled in µm. The colour bar unit is counts per second. **b** The CW ODMR measurements of the eight NV sensors (NV 1–8) in parallel under zero field. Microwave frequency is abbreviated as MW. freq. **c** Experimental Zeeman-splitting showing the NV ensemble response. This corresponds to simulations in (**d**). By fitting the resonance with Gaussian dip(s), the FWHM width and contrast can be extracted. **e** Characterisation of the Zeeman splitting for the eight sensors. Linear splitting is found with respect to the external magnetic field strength. **f** Characterisation of the CW-ODMR sensitivity as a function of magnetic field strength. The insensitivity (increased $\eta_{\mathrm{CW-ODMR}}$) under higher field is due to resonance broadening and reduced contrast.

$_{\mathrm{-ODMR}}$ can also be understood as the minimum DC magnetic field we can detect using CW-ODMR with 1 Hz bandwidth, and the $\sqrt{\mathrm{Hz}}$ scaling indicates that the sensitivity improves (the minimum detectable field decreases) with the square root of integration time. We characterise the magnetic field sensitivity of the eight sensors in Fig. 2f. Note that in zero field, the sensitivity $\approx 25\,\mu\mathrm{T}/\sqrt{\mathrm{Hz}}$ is similar to other NV-ensemble-based sensors[22,25]. Under 1 mT magnetic field strength, $\eta_{\mathrm{CW-ODMR}}$ increases to $\geq 50\,\mu\mathrm{T}/\sqrt{\mathrm{Hz}}$ and doubles again to $\geq 100\,\mu\mathrm{T}/\sqrt{\mathrm{Hz}}$ under 1.5 mT due to increased ensemble broadening and reduced resonance contrast, as shown in Fig. 2c, d. The experimental data points are compared with extracted values from fitted ensemble sensor models (solid lines).

The full operating window of the sensors, however, extends from 0.2 mT to 2.2 mT (see below and Supplementary Section C). For $|B| < 0.2$ mT, the Zeeman splitting is insensitive to external fields due to strain in the nanodiamond, while the ODMR contrast decreases significantly to ≤1% for $|B| > 2.2$ mT. Compared with single-NV CW-ODMR sensitivity around $1\,\mu\mathrm{T}/\sqrt{\mathrm{Hz}}$[26] and NV-ensemble sensitivity around $10\,\mathrm{nT}/\sqrt{\mathrm{Hz}}$[27], the 10–100 $\mu\mathrm{T}/\sqrt{\mathrm{Hz}}$ sensitivity reported here has room for optimisation via improved diamond quality, higher pump power, and advanced magnetometry protocols (see Conclusions). As the sensitivity of the sensor scales with $1/\sqrt{R}$, and we operate with < 0.2 mW pump power per site, below the saturation power (> 4 mW as shown in ref. 15), one can further increase the sensitivity (decrease

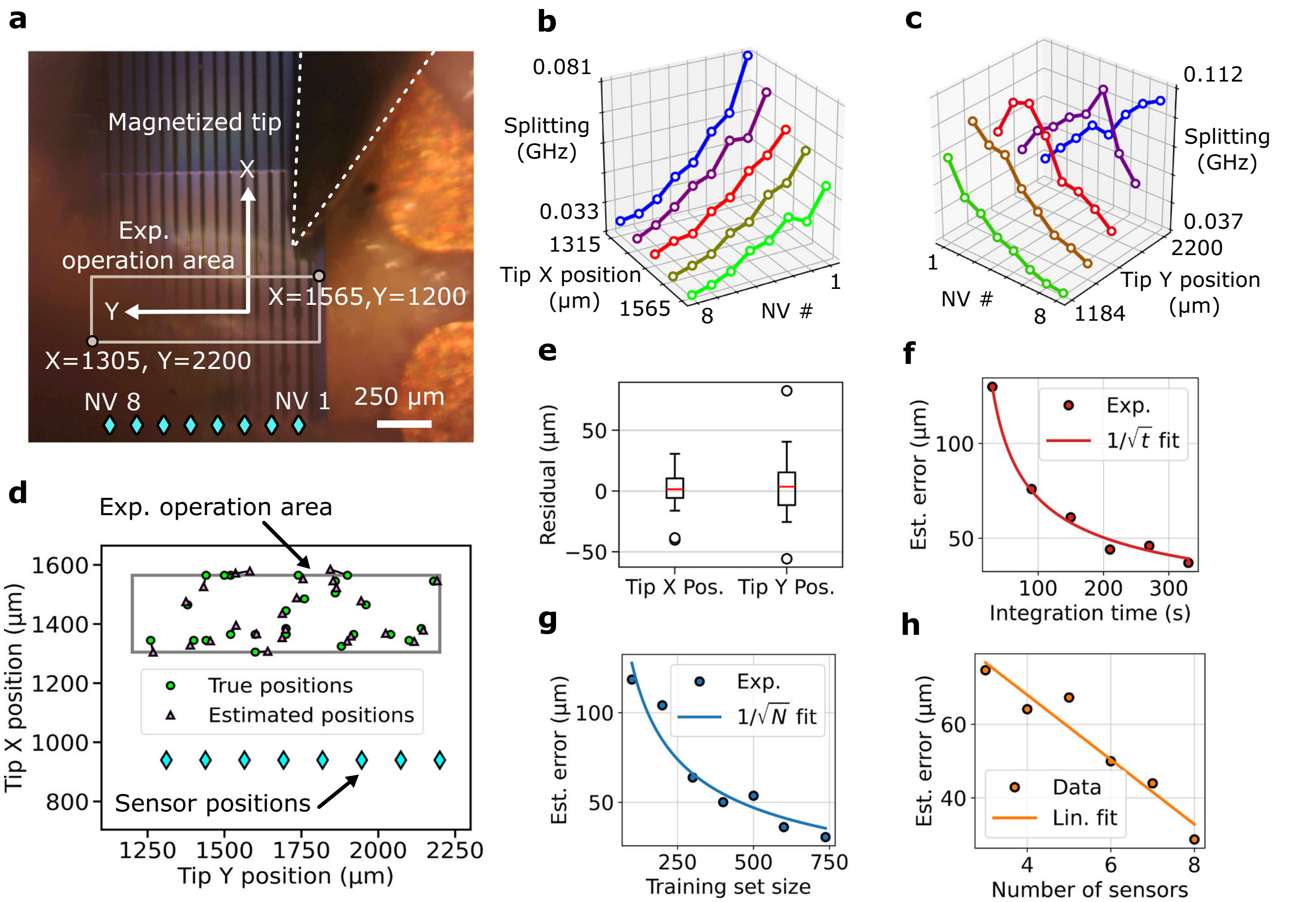

Fig. 3 | Experimental magnetic localisation with multi-point field reconstruction. a Image showing the magnetic needle tip above the chip, the experimental (exp.) operation area, and the sensor relative positions. Note that the same X-Y coordinates (the needle tip motor stage reference frame) in μm are used throughout this figure. The NV-ensemble sensors characterised in Fig. 2 are used. The Zeeman splittings of each NV sensor when the tip moves in the X direction, showing an increased gradient. **c** The Zeeman splittings recorded when the tip moves in the Y direction, showing the translation in peak field position. **d** Experimental magnetic localisation. The sensor array is used to estimate the needle position in X and Y. The experimental operation area is enclosed by the grey box with the sensor positions labelled. **e** Residual analysis for the magnetic localisation result in (**d**), comparing the needle tip X and Y positions. **f** The $1/\sqrt{t}$ scaling of the average estimation error with the integration time t. **g** Relationship between average estimation error and training dataset size N, showing $1/\sqrt{N}$ scaling. Measurements are done with a 360 s integration time. **h** The linear decrease of the averaged estimation error with increased number of sensors used simultaneously. The full training data set and a 360-s integration time are used.

$\eta_{CW-ODMR}$) by pumping the sensors harder and potentially detecting the signal with low-noise photodiodes as opposed to single-photon detectors.

Static magnetic localisation through multi-point field reconstruction

By operating the eight spatially resolved magnetic magnitude sensors at the same time, we first show imaging of a gradient field. The gradient field (at a few μT/μm level) is generated by a magnetised needle tip placed close to the sensors (Fig. 3a). The needle tip is 30 μm in diameter, kept at a distance of 250 μm above the chip, and tilted at a 45° angle (see Supplementary Section D). When the tip is directed towards NV sensor 1 (NV 1), moving the tip closer (in the negative X direction of Fig. 3a), increases field gradient across the sensors (Fig. 3b). Conversely, when the tip moves across the waveguides (in the positive Y direction of Fig. 3a) while maintaining its distance from the sensors, one can see the change in peak field location, moving from NV sensor 1 (NV 1) to NV sensor 8 (NV 8) in Fig. 3c. The ability to image a gradient field in real time implies that the eight sensors are recording distinct and localised magnetic fields in parallel, and can be used for multi-point field reconstruction.

Through multi-point field reconstruction, the relations between sensor readouts can be used to estimate the needle tip position from a magnetic inverse calculation, i.e., to implement magnetic localisation. Localising a DC/AC magnetic source is a core technique in many bioimaging[28] and engineering[29] methods. Magnetic localisation, different from direct wide-field imaging[30,31], (1) does not require direct optical access to the target (since the target's field is recorded remotely by the sensors), and (2) has ultimate resolutions fundamentally limited only by the physical size of the sensors (similar to the localisation method used in ref. 7). We utilise a Convolutional Neural Network (CNN)-based method (see details in Methods) for the magnetic inverse calculation. The machine learning method, also commonly used in biomedical magnetic inverse imaging[32] and geophysical magnetic source localisation[33], is chosen for generalisation compared to simple field inversion, especially when the magnetic field distribution of the source is unknown or hard to fully characterise. Also, the CNN-based model, in contrast to a simple deep neural network, can better capture the relation between spatially-structured sensor readouts for comparison. The model is trained with 737 labelled experimental data points, sampled across an area of 260 μm by 1000 μm (the grey box in Fig. 3a), to learn the X-Y position of the needle tip by the Zeeman splittings of the eight sensors along with the standard deviation of fitted resonance frequencies in the ODMR measurements. The centre of the area is chosen about 500 μm from the sensors such that the field gradient is strong enough to show distinct trends (as in Fig. 3b and c), but the field strength stays within the low field regime to operate with reasonable sensitivities.

In Fig. 3d, we test the trained CNN model with data points unused in the training process, comparing the estimated positions (pink triangular data points) with the true positions of the needle tip (cyan circular data points). The data points are paired up with connection lines to show the estimation error. The operation area and the sensor positions are also labelled in the same figure for reference. We observe an average of 23 μm estimation error, which falls within the tip size of 30 μm (see Supplementary Section D). The position estimation shows a slightly larger error in Y positions compared to the X positions since the magnetic gradient is smaller in the Y direction (see Supplementary Section D). Figure 3e shows the X and Y residuals with an interquartile range of 16 μm and 27 μm, respectively. The outliers are cases where a misalignment in the setup caused drops in the PL signal. Note that for each data point here, we integrate the ODMR measurements for 360 s.

The estimation error is affected by various experimental parameters. For example, by integrating the ODMR measurements for a shorter period of time, the localisation estimations can be made faster, however, at a higher noise level. We show the scaling between integration time t and estimation error in Fig. 3f, which matches a $1/\sqrt{t}$ fitting as expected for the shot noise in photon counting. To see how much training data is needed for machine-learning based magnetic localisation, we analyse how the averaged estimation error scales with the dataset size N in Fig. 3g. The estimation error follows $1/\sqrt{N}$ scaling. This is expected since, with fixed operation area A, $\sqrt{A/N}$ presents the resolution of sampled data points (with length unit). Using more sensors for magnetic localisation allows us to collect more data simultaneously, which improves the reconstruction of the magnetic field. This advantage is captured by Fig. 3h, showing that the estimation error reduces linearly with the number of sensors used. To understand the linear relation, one should first note that the useful information for the machine learning model is the number of pair-wise correlations (which scales with n^2) that can be extracted from n sensors, similar to the mathematical principle behind correlated and covariance sensing[7,9]. One should also note that higher-order correlations can, in principle, provide more information in magnetic localisation. As a result, the $1/\sqrt{N}$ scaling for data sizes becomes $1/\sqrt{n^2} = 1/n$ for the number of sensors.

The position estimation error, symbolising the practical magnetic-localisation resolution, is determined by factors beyond the physical size of the sensor (a few μm in our case), such as the sensor sensitivity and the local magnetic field gradient. To understand the relation, we model the spatially-averaged error $\overline{R}_{x,y}$, by averaging the position-dependent error $R_{x,y}$ over the sample area where

$$R_{x,y} \approx \frac{S_{x,y}}{\sqrt{t}\, m_{x,y}}. \tag{2}$$

Here, $S_{x,y}$ is the sensor sensitivity at position (x, y), t is the integration time for the ODMR measurements, and $m_{x,y}$ is the field gradient generated by the magnetic source. From the sensor sensitivities in Fig. 2f, the integration time (360 s), and the field gradient generated by the tip (see Supplementary Section D) in the Fig. 3d operation area, we estimate $\overline{R}_{x,y} \approx 22.5\,\mu$m, with an averaged error in the x direction of 10.6 μm and 17.9 μm in the y direction. This is in good agreement with the experimentally observed 23 μm averaged error in Fig. 3d and the larger Y position error in Fig. 3e.

Dynamics of a moving magnetic source: continuous-time tracking

Beyond localising stationary magnetic objects, we can use the eight sensors to track a moving target in continuous time. To demonstrate this, we programme the motor stage such that the needle tip follows an S-shaped trajectory in 100 steps, with a speed of 7.1 μm/min, 3.5 μm/min, 1.8 μm/min (defined by the 10.6 μm step size and the 90 s, 180 s, and 360 s dwell time at each position). The ODMR measurements of the eight sensors are taken continuously to record the dynamics of the needle tip. The trajectory is then reconstructed with frame rates of 2.8 mHz, 5.6 mHz, and 11.1 mHz (defined by one over the 360 s, 180 s, and 90 s integration time). The results are shown in Fig. 4, with the red curve showing the true trajectory and the connected data points giving the reconstructed trajectory. When the needle tip speed increases and the frame rate is fixed, we observe a smeared trajectory due to undersampling (tip moved multiple steps within one frame/measurement). For example, a large deviation from the true trajectory can be seen in Fig. 4c, especially where the curvature is large, compared to Fig. 4b and a. On the other hand, comparing Fig. 4d–f, when the needle tip moves at a certain speed, a noisier trajectory is observed at higher frame rates (as expected from Fig. 3f due to shot noise). To quantify the fidelity of the trajectory reconstruction, we calculate the error in terms of the Mean Perpendicular Distance (MPD), i.e., the averaged shortest distance from each estimated data point to the true trajectory. Note that the stationary averaged estimation error is not used as the metric here because the movement is typically not synchronised with the ODMR measurement integration time in tracking unknown dynamics (i.e. the magnetic localisation can be performed while the tracked object moves, depending on the frame rate chosen). We can observe an increased MPD for under sampling in Fig. 4c (due to smearing when the integration time is longer than the dwell time). In Fig. 4e, f, the MPD also increases due to shot noise. Supplementary Section F visualises both effects at the same time with MPD calculated.

Magnetic microrobot tracking- simulations and the use of single-NV sensors

Our platform enables (i) a multi-NV sensing architecture without the use of complex bulk optics, and (ii) a microscale localisation technique without need for direct optical access to the target, presenting a practical and deployable solution for real-life quantum sensing applications. Here, we show in simulation one such application: dynamical tracking of in-plane magnetic microrobot dynamics, for many clinical and biomedical purposes[16,17,34,35]. The concept is shown in Fig. 5a, where our magnetic localisation technique can help navigate a magnetically-driven microrobot in an optically-inaccessible environment for a drug-delivery mission[35]. Note that machine learning models can first be trained outside the test body[36]. The same type of microrobots can then be deployed to the optically inaccessible environments. Also, the magnetic field used to drive the microrobot is homogeneous across the sensors, whose contribution can be easily eliminated in the magnetic localisation calculations.

For microrobot tracking applications, it is crucial to characterise the valid spatial range of operation. We show this by simulation (see details in Supplementary Section H), considering a magnetic hydrogel microrobot made of Fe_3O_4 particles[16] with a diameter of 100 μm, whose magnetic profile is simulated by COMSOL Multiphysics. Note that the simulation considers the NV ensemble quantum sensor sensitivity in Fig. 2, the ODMR integration time of 360 s, and the photonic layout in Fig. 1. In Fig. 5b, we show the position-dependent error map of the microrobot localisation, calculating the estimation error for positions sampled over a 1400 μm by 1400 μm area. Within a good operation area of 750 μm by 1400 μm (as shown by the contour line), we observe ≤50 μm estimation error. The estimation error is captured by Eq. (2)–the magnetic localisation fails when the microrobot moves too far away from the sensors, and thus the magnetic field gradient is

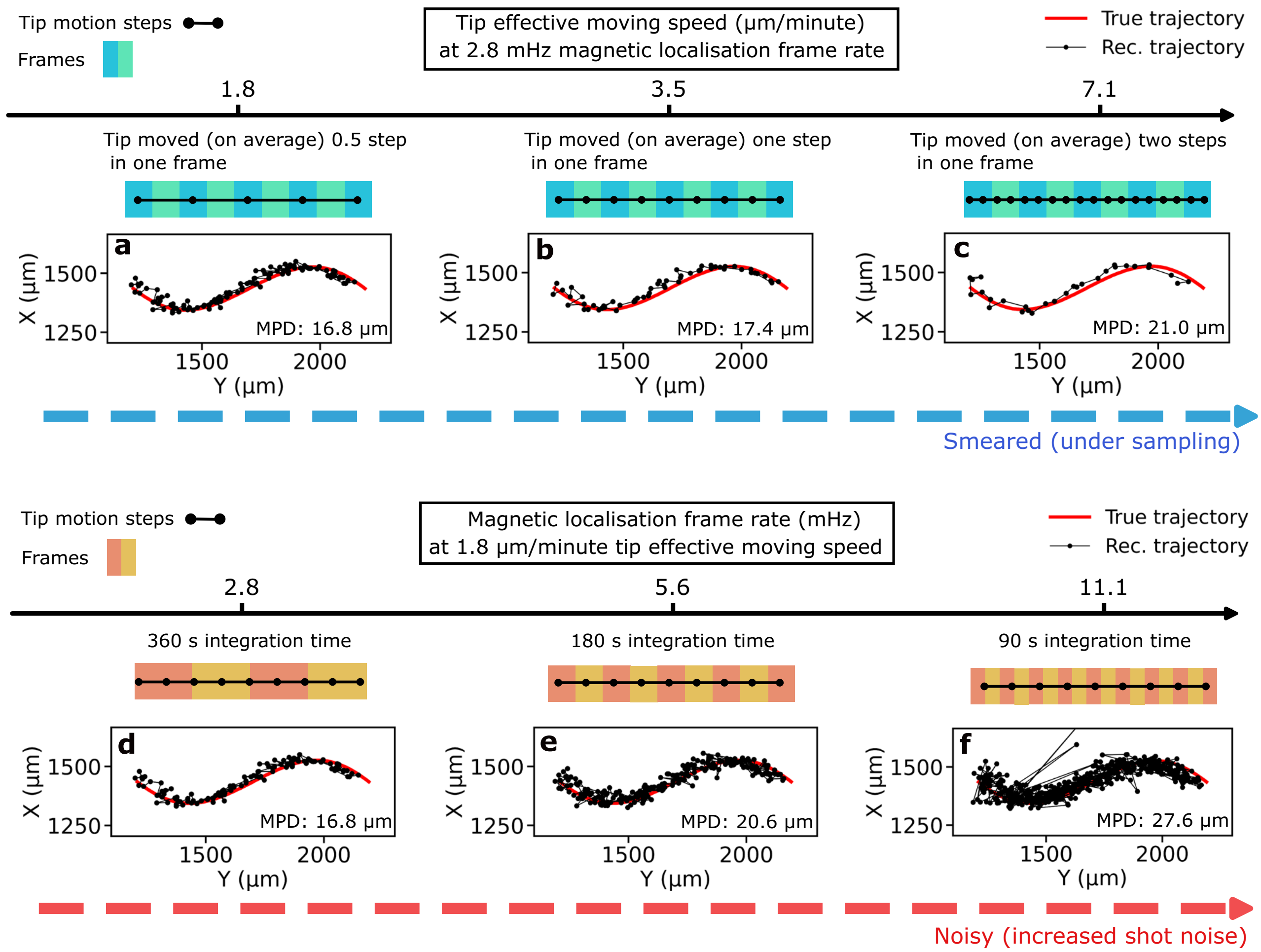

Fig. 4 | Experimental dynamical tracking of moving magnetic object. The needle tip, when programmed to move at different speeds (effective speeds are calculated from step size divided by the dwell time), is tracked with different frame rates for comparison. **a**–**c** compare the tracking at different tip moving speeds, while **d**–**f** present tracking with different frame rates. Note that the same machine-learning model is used for magnetic localisation and the trajectory falls within the operation area in Fig. 3a. Note that **a**, **d** show the same data. The deviation of the reconstructed (rec.) trajectory from the true trajectory is quantified by the Mean Perpendicular Distance (MPD), which increases for higher moving speeds due to under sampling (tip moved multiple steps in one frame) and higher frame rates due to shot noise, as illustrated by the diagrams.

significantly reduced. This argument is supported by the statistics shown in Fig. 5c, plotting the y-averaged estimation error in different robot X positions. The anti-correlation between the averaged field gradient at the NV sensors and the estimation error is observed. When the gradient falls below 0.008 mT/μm, the localisation error exceeds 50 μm (see Fig. 5c), defining the boundary of the good operation area at x = −750 μm. This gradient threshold sets the maximum tracking distance and depends on both sensor sensitivity and integration time. Note that the decreased $m_{x,y}$ dominates over decreased $S_{x,y}$ here (due to resonance broadening), as the NV ensemble sensors are kept reasonably far away in z with a standoff of 250 μm. Also, this position dependence is not obvious in Fig. 3d as a smaller operational area (span in the Fig. 3a X direction) is explored due to physical constraints in the experimental setup.

We further consider the use of single NVs as quantum sensors integrated with photonic waveguides for magnetic localisation. Single NVs have been integrated in similar platforms[15], and we also show that CW ODMR and coherent spin operation (Rabi oscillations) are possible experimentally (see Supplementary Section G). An array of single-NV sensors can be created (as shown in Supplementary Section I). A single NV sensor, with a much weaker optical signal but narrower resonance linewidth, is measured with a 25 $\mu T/\sqrt{Hz}$ CW ODMR sensitivity under a weak unaligned external field. The single NV sensitivity can degrade under unaligned fields due to spin mixing and quenching[37] but less significantly in the low field regime (< 5 mT) compared to NV ensembles (as shown in Fig. 2f). Also, positioned single NVs in nanodiamonds naturally have different orientations that can be used collectively to provide vectorial information of the magnetic field. We show in simulation (Fig. 5d) that the position of the same 100-μm microrobot can be tracked by eight single NV sensors, with an average estimation error of ≤10 μm (see details in Supplementary Section H). In this simulation, the single NV sensitivity (along with random orientations), the same photonic scheme, and 360 s of ODMR integration time are considered. Furthermore, the controlled rotation of the microrobot along the trajectory (Fig. 5e) can be simultaneously monitored, with $\delta_\theta \approx 5^\circ$ average estimation error.

Discussion

In this work, we introduce multi-NV quantum sensing using foundry silicon-nitride integrated photonic circuits. The uniformly positioned NV sensors are controlled by parallel fibres and read out through distinct waveguides. Enabled by multi-point field reconstruction with the eight NV sensors in an array, we experimentally demonstrate magnetic localisation of a 30 μm needle tip with error below its dimension and dynamic tracking of the tip position. We further present, by simulation, the potential of our platform for position and

https://doi.org/10.1038/s41467-026-73701-0

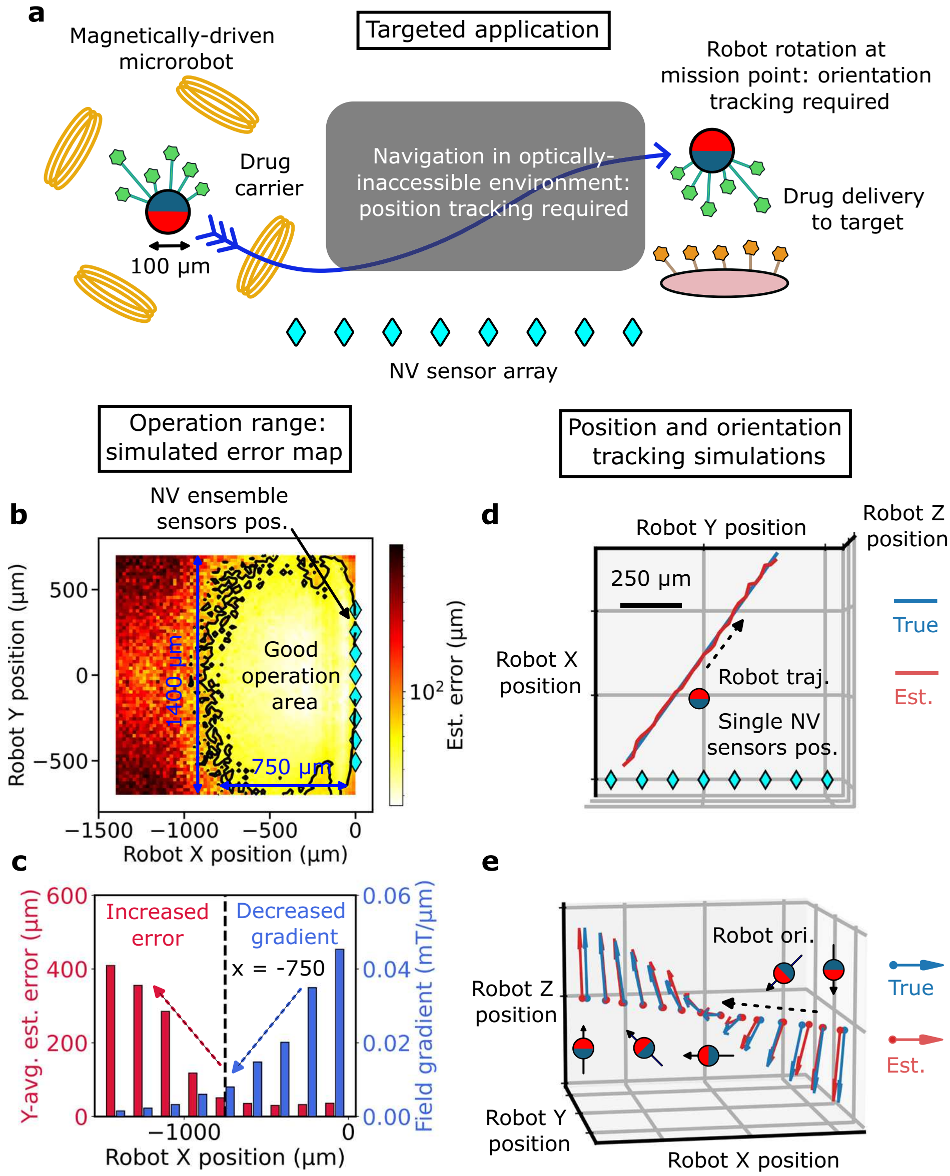

Fig. 5 | Application to position and orientation tracking of magnetically-driven microrobot. a Targeted application scenario. The cartoon diagram shows that a 100-μm sized magnetically-driven microrobot, on a mission of pin-point drug delivery, requires the ability to navigate through optically-inaccessible environments with precise control. With our magnetic localisation technique, the microrobot can be efficiently localised and tracked when performing biomedical tasks using an array of NV ensemble or single-NV sensors. Panels (**b**–**e**) use simulation to connect the demonstrated sensing modality and geometry to application-relevant operating requirements. **b** Error map of simulated microrobot magnetic localisation, with eight ensemble NV sensors. The robot-position-dependent estimation error is plotted with the relative positions of the NV ensemble sensors labelled. The good operation area (with estimation error ≤50 μm) is shown by the contour line. **c** The y-averaged estimation error and the averaged magnetic field gradient at the sensor locations for different robot x positions. When the robot moves away from the sensors, the estimation error increases as a result of decreased field gradient. See also Supplementary Section H for the microrobot magnetic field profile. The dashed vertical line at x = −750 μm shows where the good operation range is defined (when estimation error stays ≤50 μm). **d** Position tracking of the microrobot along a trajectory (abbreviated as traj.) with eight single NV sensors. The single-NV sensor positions are labelled. We consider the single NV sensors only 150 μm below the microrobot since their superior sensitivity at higher field allows the robot to be tracked with a smaller z standoff. **e** Monitoring of microrobot rotations. The change of orientations (abbreviated as ori.) alongside the trajectory (as visualised by the robot diagram) can be precisely tracked with the single NV sensors. Arrows in the plot show the true and estimated orientations for every two points along the trajectory.

orientation monitoring of magnetic microrobots for biomedical applications.

The frame-rate requirements (F) for tracking moving microrobots are determined by both motion speed (v) (to avoid undersampling) and the desired localisation accuracy (δ_L) i.e., $F \gtrsim v/\delta_L$. Under the present CW-ODMR regime (360 s integration, $F \approx 2.8$ mHz) and the $\delta_L \le 50\,\mu$m localisation precision observed in our ensemble-sensor demonstrations (and used in the microrobot case-study simulation), this implies a characteristic trackable speed $v \lesssim 0.14\,\mu$m/s. For context, microrobot speeds span roughly 0.1–10 μm/s[16,17]. For high-speed scenarios (e.g., v ~ 600 μm/s to 1 mm/s), avoiding undersampling at $\delta_L = 50\,\mu$m would require $F \gtrsim 12$–20 Hz, i.e., effective integration times $\lesssim$ 50–80 ms, far beyond the present CW-ODMR demonstration. This quantitative bound highlights the central speed–accuracy trade-off and provides a clear benchmark for translating integrated multi-sensor localisation from minute-scale dynamics to faster regimes.

Rotation tracking further requires vector information (e.g., single NVs or oriented ensembles). Using the single-NV simulation in

Fig. 5e with $\delta_\theta \approx 5^\circ$, an analogous requirement $\Omega \lesssim F\delta_\theta$ gives $\Omega \lesssim 2.4\times10^{-4}$ rad/s at $F\approx 2.8$ mHz, underscoring that substantially faster rotation tracking[38,39] would require much shorter effective integration times and higher effective sensitivity.

Looking forward, extending the demonstrated integrated architecture to substantially faster or rotation-aware tracking will require major reductions in integration time through higher sensitivity and duty cycle (e.g., via improved spin resources and/or pulsed protocols), while accounting for practical overheads (i.e., thermal constraints). Maintaining $\delta_L \sim 50\,\mu$m at $F\sim 10$–20 Hz implies $\sim 10^4$ shorter integration than our current 360 s demonstrations; under Eq. (2), this corresponds to $\sim 10^2$ improvement in effective sensitivity at fixed gradient. For context, nT/$\sqrt{\text{Hz}}$-level sensitivities have been demonstrated with NV ensembles under optimised conditions and protocols[27,40], indicating a plausible pathway to orders-of-magnitude improvements beyond the present on-chip nanodiamond CW-ODMR regime. Notably, the system-level advance demonstrated here—simultaneous, distinct, multi-channel readout of spatially separated NV sensors on a fibre-addressed photonic platform—provides a scalable hardware foundation (requiring photonic mode engineering similar to ref. 41) on which such sensing-protocol improvements can be deployed.

The sensor array is also scalable. For example, one can extend the operation range by (a) increasing the number of sensors in the current line and (b) adding a parallel array to the current one. The enlarged array can be controlled with commercial fibre arrays, with up to 96 fibres and the same 127 μm spacing. This could extend the operation Y range in Fig. 5c by more than ten times to $\approx$15 mm. A second parallel array, on the other hand, doubles the operation X range in Fig. 5c. On top of that, by improving the sensor sensitivity to around 1 nT/$\sqrt{\text{Hz}}$ level (which we show in Supplementary Section I is possible by leveraging high-density NV ensembles with μs-level T_2^* coherence time), one can simultaneously increase the frame rate by 10^4 times and the operation range by another 10 times (see also Supplementary Section I for detailed calculations). Spin addressing over an extended area (at 10 mm scale) can be achieved with specially designed microwave antennas[21,42,43]. Notably, with the number of sensors significantly increased, machine learning-based methods become the only way to efficiently extract the correlations between sensor readouts for magnetic inverse calculation. In contrast, to track smaller magnetic robots (such as nanowire robots of overall length 5–10 μm[44]), sensor arrays with spacing ten times smaller (around 10–20 μm) can be achieved by bringing the parallel waveguides closer in the sensor region and optical excitation with multi-core fibres[45].

Our platform, based on commercial silicon photonics, demonstrates scalability and stability compared to direct-written diamond waveguides[40] and single-mode fibre assemblies[46] for out-of-the-lab quantum sensing conditions. The deterministically positioned NVs also allow static control with fibre arrays and waveguides, in contrast to stochastic sensors that need to be addressed by fast programmable optics[11,12]. Machine-learning-based localisation, similar to what was found in ref. 47, extends to micrometre-sized objects. Our platform can also be adopted for other multi-NV sensing protocols[9,14] for different use cases. Moreover, with improved photonic architecture, NV ensembles could be pumped via in-plane waveguide channels[48], thereby freeing access to the space above the sensors. With complete photonic packaging, chip-based quantum sensing could facilitate clinical and biomedical applications where bulk optical imaging is impractical[49,50].

Methods

Experimental setup

Here, we include details of the experimental setup. The photonic chip is fabricated by IMEC (BioPIX silicon nitride 150 nm platform). The fibre arrays used for pumping the NV and collection of PL from both sides are made by Oz Optics and Precision Micro-Optics, with eight PM630 polarisation-maintaining single-mode fibres in a V-groove array separated by 127 μm. The excitation fibre array is mounted on a scanning stage with a tip, tilt, and rotation stage (TTR001/M Thorlabs), whereas the collection fibre arrays are mounted on six-axis stages (Nanomax Thorlabs). The NV centres are pumped by a 40-mW CW Cobolt 06-MLD laser. The NV spins are driven by a microwave source (SMB100AP20 Rohde & Schwarz), amplified by microwave amplifiers (AM4-2-6-43-43R Microwave Amplifiers Ltd) and delivered by a PCB grounded coplanar waveguide antenna. The PL signal from eight sensors passes through a notch filter (NF03-514E-25 Semrock) and long pass filter (BLP01-568R-25 Semrock). With a pair of fibre bundles (BF74HS01 Thorlabs), the same optical filters can be shared by up to seven individual beam paths. Through the fibre bundle and filter sets, we measure an averaged 65% efficiency for the PL signal in the transmission band and an average of < 0.1% crosstalk between fibre channels. Eight single-photon avalanche diodes (SPCM-AQRH-12-FC Excelitas) are used for PL detection. The timetags are recorded by a Logic-16 (UQDevices), where eight out of sixteen channels are used for data processing at the same time. In ODMR measurements, the Pulse Streamer 8/2 (Swabian Instruments) is used to trigger the microwave source and synchronise with the photon counting. The ODMR is set with a dwell time of 1 ms on each frequency to ensure fast data processing. The excitation fibre array is scanned by a motorised three-axis stage, positioned a few microns away from the chip surface to ensure efficient excitation power density. Note that the photonic coupling (fibre to waveguide) and bulk optics efficiency remain stable for weeks with only minimal tuning needed.

Nanodiamond positioning

The nanodiamond positioning method follows ref. 15 with minor differences. The photonic chip is first covered by a polymethyl methacrylate (PMMA) mask, on which the deposition sites are written with electron beam lithography (Raith Voyager). After development, this creates precisely defined windows on the waveguide for nanodiamond positioning. The fluorescent nanodiamond (brFND-100 FND Biotech) is suspended in deionised water (at 1 mg/ml concentration), followed by 2-h ultrasonication and filtering with 0.45 μm syringe filters. Drops of the nanodiamond suspension are then pipetted on the deposition area (red middle region in Fig. 1c) and dried at room temperature. The dropcasting is repeated five times to ensure proper coverage over the area. The residual nanodiamonds on the mask are removed during the lift-off of PMMA in acetone, followed by a gentle ultrasonication for 10 s. Only the nanodiamonds attached to the waveguides over the patterned sites remain.

NV ensemble simulations

For NV ensembles in nanodiamonds, we simulate CW ODMR measurements based on ref. 22. For a single NV, the electron spin resonance frequencies are $\nu_{\pm1} = D \pm \sqrt{E^2 + (\gamma\vec{B}\cdot\hat{a})^2}$, where E captures the effect of strain in the nanodiamond, γ is the NV gyromagnetic ratio $\approx$ 28 GHz/T, $\vec{B}$ is the external magnetic vector field, and $\hat{a}$ is the unit vector along the NV axis. Each resonance in the CW ODMR can be presented by a Gaussian dip $1 - G(\nu, \delta\nu, C)$, where ν is the central frequency, $\delta\nu$ is the associated resonance linewidth, and C is the contrast. Considering an NV ensemble with isotropic distribution of orientations, the collective response can be modelled by $1 - n\int_0^\pi [G(D - \sqrt{E^2 + (\gamma|B|\cos\theta)^2}, \delta\nu, C) + G(D + \sqrt{E^2 + (\gamma|B|\cos\theta)^2}, \delta\nu, C)]\sin\theta\, d\theta$, where θ considers the orientation averaging and n is a normalisation factor. Here, we assume no angular and spin dependence for the NV fluorescence, contrast C, strain E, and linewidth $\delta\nu$, as well as homogeneity of these parameters in the ensemble. These parameters (with an average of E = 5.6 MHz, C = 3.4%, and $\delta\nu$ = 14.7 MHz across the eight NV ensemble sensors) are decided experimentally by fitting the CW ODMR results in Fig. 2c. These results are found similar to those in ref. 22.

Machine learning methods for experimental magnetic localisation

For magnetic localisation, we adopt a Convolutional Neural Network (CNN)-based machine-learning method for the magnetic inverse calculation. The machine-learning-based method is suitable for scenarios where the magnetic field profile of the source is hard to characterise or often changing. For a different target (or a change of the magnetic profile), one needs to retrain the model for optimal estimation precision. Also, certain physical bounds on the target movement have to apply (for example, movement only in the xy plane with fixed z), to avoid position redundancy that cannot be differentiated by magnetic fields. This needs to be more carefully considered, especially when magnitude sensors are used (such as the NV ensemble sensor based on nanodiamonds), compared to single-NV sensors, due to the lack of vectorial field information.

Here, we provide details on the CNN model used to achieve magnetic localisation in Figs. 3, 4. During data preprocessing, we fit the CW ODMR measurement results (after a two-point smoothing filter) by a double-gaussian-dip function to extract the Zeeman splitting (difference of the two resonance frequencies) as well as the fitting standard deviation for the two resonances for all eight sensors. Note that we take the natural logarithm of these values so that the difference between sensors is more easily captured by the model. The labelled data is split such that 90% is used for training, 7% is used for validation while training, and 3% is used for testing and visualisation in Fig. 3d. The train-validation-test separation of the dataset is shown in Supplementary Section E. The CNN-based model is implemented using TensorFlow, starting with three Conv1D layers of 64, 128, and 256 dimensions, each followed by a ReLU activation function. Three Dense layers are then used (of 128, 64, and 2 dimensions) after flattening. An Adam optimiser is used with a learning rate of 0.005, and the model is trained for 3000 epochs under a batch size of 128. The training is monitored with a validation dataset and stopped before overfitting happens. This training can be easily done with a laptop in less than 30 min. Once trained, the same model can be used for magnetic localisation as long as experimental conditions are maintained (the magnetic needle tip setup and orientation). The magnetisation of the needle tip also remains constant throughout the experiments. See Supplementary Section D for details of the magnetic needle tip setup.

More details on machine learning models used for the microrobot simulation can be found in the Supplementary Section H.

Data availability

The data that supports the plots within this paper and that is used to train the machine learning model is available at the Zenodo repository[51]. Any additional materials and data are available from the corresponding authors upon request.

Code availability

The codes that generate the plots within this paper and that are associated with the machine learning model are available at the Zenodo repository[51].

References

1. Rovny, J. et al. Nanoscale diamond quantum sensors for many-body physics. *Nat. Rev. Phys.* **6**, 753–768 (2024).
2. Casola, F., Van Der Sar, T. & Yacoby, A. Probing condensed matter physics with magnetometry based on nitrogen-vacancy centres in diamond. *Nat. Rev. Mater.* **3**, 1–13 (2018).
3. Aslam, N. et al. Quantum sensors for biomedical applications. *Nat. Rev. Phys.* **5**, 157–169 (2023).
4. Balasubramanian, G., Lazariev, A., Arumugam, S. R. & Duan, D. -w Nitrogen-vacancy color center in diamond–emerging nanoscale applications in bioimaging and biosensing. *Curr. Opin. Chem. Biol.* **20**, 69–77 (2014).
5. Le Sage, D. et al. Optical magnetic imaging of living cells. *Nature* **496**, 486–489 (2013).
6. Briegel, K. D. et al. Optical widefield nuclear magnetic resonance microscopy. *Nat. Commun.* **16**, 1281 (2025).
7. Ji, W. et al. Correlated sensing with a solid-state quantum multisensor system for atomic-scale structural analysis. *Nat. Photonics* **18**, 230–235 (2024).
8. Delord, T., Monge, R. & Meriles, C. A. Correlated spectroscopy of electric noise with color center clusters. *Nano Lett.* **24**, 6474–6479 (2024).
9. Rovny, J. et al. Nanoscale covariance magnetometry with diamond quantum sensors. *Science* **378**, 1301–1305 (2022).
10. Huxter, W. S., Dalmagioni, F. & Degen, C. L. Multiplexed scanning microscopy with dual-qubit spin sensors. *Phys. Rev. Lett.* **135**, 153801 (2025).
11. Cheng, K.-H. et al. Massively multiplexed nanoscale magnetometry with diamond quantum sensors. *Phys. Rev. X* **15**, 031014 (2025).
12. Cambria, M., Chand, S., Reiter, C. M. & Kolkowitz, S. Scalable parallel measurement of individual nitrogen-vacancy centers. *Phys. Rev. X* **15**, 031015 (2025).
13. Le, X. H. et al. Wideband covariance magnetometry below the diffraction limit. *Phys. Rev. Lett.* **135**, 170803 (2025).
14. Yoon, J. et al. Quantum sensing with arbitrary frequency resolution via correlation measurements. *arXiv* https://doi.org/10.48550/arXiv.2504.12134 (2025).
15. Weng, H.-C. et al. Heterogeneous integration of solid-state quantum systems with a foundry photonics platform. *ACS Photonics* **10**, 3302–3309 (2023).
16. Jiang, F. et al. Magnetic propelled hydrogel microrobots for actively enhancing the efficiency of lycorine hydrochloride to suppress colorectal cancer. *Front. Bioeng. Biotechnol.* **12**, 1361617 (2024).
17. Wrede, P. et al. Real-time 3d optoacoustic tracking of cell-sized magnetic microrobots circulating in the mouse brain vasculature. *Sci. Adv.* **8**, 9132 (2022).
18. Jeon, S. et al. A magnetically powered stem cell-based microrobot for minimally invasive stem cell delivery via the intranasal pathway in a mouse brain. *Adv. Healthc. Mater.* **10**, 2100801 (2021).
19. Wojciechowski, A. M. et al. Optical magnetometry based on nanodiamonds with nitrogen-vacancy color centers. *Materials* **12**, 2951 (2019).
20. Tiwari, V. et al. Single photon emission from lithographically-positioned engineered nanodiamonds for cryogenic applications. arXiv https://doi.org/10.48550/arXiv.2508.06424 (2025).
21. Weng, H.-C., Rarity, J.G., Balram, K.C., Smith, J.A. Crosstalk-mitigated microelectronic control for optically-active spins https://arxiv.org/abs/2404.04075. (2025).
22. Foy, C. et al. Wide-field magnetic field and temperature imaging using nanoscale quantum sensors. *ACS Appl. Mater. interfaces* **12**, 26525–26533 (2020).
23. Hui, Y.Y., Tsui, Y.-M., Tang, Y.-X., Chang, H.-C. Ultrathin fluorescent nanodiamond films for nanoscale quantum sensing in operando semiconductor devices. *Advanced Functional Materials*, https://doi.org/10.1002/adfm.202513406 (2025).
24. Barry, J. F. et al. Sensitivity optimization for NV-diamond magnetometry. *Rev. Mod. Phys.* **92**, 015004 (2020).
25. Kim, D. et al. A cmos-integrated quantum sensor based on nitrogen–vacancy centres. *Nat. Electron.* **2**, 284–289 (2019).
26. Dréau, A. et al. Avoiding power broadening in optically detected magnetic resonance of single NV defects for enhanced DC magnetic field sensitivity. *Phys. Rev. B–Condens. Matter Mater. Phys.* **84**, 195204 (2011).

27. Zhang, Y. et al. High-sensitivity DC magnetic field detection with ensemble NV centers by pulsed quantum filtering technology. *Opt. Express* **28**, 16191–16201 (2020).
28. Flynn, E. & Bryant, H. A biomagnetic system for in vivo cancer imaging. *Phys. Med. Biol.* **50**, 1273 (2005).
29. Pasku, V. et al. Magnetic field-based positioning systems. *IEEE Commun. Surv. Tutor.* **19**, 2003–2017 (2017).
30. Mathes, N. et al. Nitrogen-vacancy center magnetic imaging of fe 3 o 4 nanoparticles inside the gastrointestinal tract of Drosophila melanogaster. *Nanoscale Adv.* **6**, 247–255 (2024).
31. Chen, S. et al. Immunomagnetic microscopy of tumour tissues using quantum sensors in diamond. *Proc. Natl. Acad. Sci.* **119**, 2118876119 (2022).
32. Jin, K. H., McCann, M. T., Froustey, E. & Unser, M. Deep convolutional neural network for inverse problems in imaging. *IEEE Trans. image Process.* **26**, 4509–4522 (2017).
33. Puzyrev, V. Deep learning electromagnetic inversion with convolutional neural networks. *Geophys. J. Int.* **218**, 817–832 (2019).
34. Wu, D. et al. Femtosecond laser–assisted printing of hard magnetic microrobots for swimming upstream in subcentimeter-per-second blood flow. *Sci. Adv.* **11**, 1272 (2025).
35. Han, M. et al. Janus microparticle-based targeted and spatially-controlled piezoelectric neural stimulation via low-intensity focused ultrasound. *Nat. Commun.* **15**, 2013 (2024).
36. Bakenecker, A. C. et al. Navigation of a magnetic micro-robot through a cerebral aneurysm phantom with magnetic particle imaging. *Sci. Rep.* **11**, 14082 (2021).
37. Rondin, L. et al. Magnetometry with nitrogen-vacancy defects in diamond. *Rep. Prog. Phys.* **77**, 056503 (2014).
38. Fu, Q., Guo, S., Zhang, S., Hirata, H. & Ishihara, H. Characteristic evaluation of a shrouded propeller mechanism for a magnetic actuated microrobot. *Micromachines* **6**, 1272–1288 (2015).
39. Alshafeei, M. E., Hosney, A., Klingner, A., Misra, S., Khalil, I. S. Magnetic-based motion control of a helical robot using two synchronized rotating dipole fields. In: 5th IEEE RAS/EMBS International Conference on Biomedical Robotics and Biomechatronics. 151–156 (IEEE, 2014).
40. Guo, Y. et al. Enhanced quantum magnetometry with a femtosecond laser-written integrated photonic diamond chip. *Nano Lett.* **25**, 8096–8102 (2025).
41. Churaev, M. et al. A heterogeneously integrated lithium niobate-on-silicon nitride photonic platform. *Nat. Commun.* **14**, 3499 (2023).
42. Chen, Y. et al. Large-area, tridimensional uniform microwave antenna for quantum sensing based on nitrogen-vacancy centers in diamond. *Appl. Phys. Express* **11**, 123001 (2018).
43. Mariani, G., Nomoto, S., Kashiwaya, S. & Nomura, S. System for the remote control and imaging of mw fields for spin manipulation in NV centers in diamond. *Sci. Rep.* **10**, 4813 (2020).
44. Zhou, H., Mayorga-Martinez, C. C., Pané, S., Zhang, L. & Pumera, M. Magnetically driven micro and nanorobots. *Chem. Rev.* **121**, 4999–5041 (2021).
45. Hout, M. et al. Reaching the pinnacle of high-capacity optical transmission using a standard cladding diameter coupled-core multi-core fiber. *Nat. Commun.* **16**, 3833 (2025).
46. Bopp, J. M. et al. Diamond-on-chip magnetic field camera for mobile imaging. *Phys. Rev. Appl.* **23**, 034024 (2025).
47. Meneses, F. et al. Machine learning-assisted tracking of magnetic objects using quantum diamond magnetometry. *arXiv* https://doi.org/10.48550/arXiv.2502.14683 (2025).
48. Wan, N. H. et al. Large-scale integration of artificial atoms in hybrid photonic circuits. *Nature* **583**, 226–231 (2020).
49. Boto, E. et al. Moving magnetoencephalography towards real-world applications with a wearable system. *Nature* **555**, 657–661 (2018).
50. Monge, M., Lee-Gosselin, A., Shapiro, M. G. & Emami, A. Localization of microscale devices in vivo using addressable transmitters operated as magnetic spins. *Nat. Biomed. Eng.* **1**, 736–744 (2017).
51. Weng, H.-C. Data/code availability for "photonic-integrated quantum sensor array for microscale magnetic localisation", https://doi.org/10.5281/zenodo.19855773 (2026).
52. Albrecht, R., Bommer, A., Deutsch, C., Reichel, J. & Becher, C. Coupling of a single nitrogen-vacancy center in diamond to a fiber-based microcavity. *Phys. Rev. Lett.* **110**, 243602 (2013).

Acknowledgements
The authors acknowledge funding support from the Engineering and Physical Sciences Research Council (EPSRC) grant QC:SCALE EP/W006685/1. JAS acknowledges his EPSRC Quantum Technology Career Acceleration Fellowship (EP/C001220/1).

Author contributions
H.C.W. and J.A.S. conceived the project. J.A.S. designed the photonic chip. H.C.W. performed the experiment and analysed the experimental data. J.A.S., K.C.B. and J.G.R. supervised the project. H.C.W. and J.A.S. wrote the manuscript. All authors discussed the results and contributed to the manuscript.

Competing interests
The authors declare no competing interests.

Additional information
Supplementary information The online version contains supplementary material available at https://doi.org/10.1038/s41467-026-73701-0.

Correspondence and requests for materials should be addressed to Hao-Cheng Weng or Joe A. Smith.

Peer review information *Nature Communications* thanks the anonymous reviewers for their contribution to the peer review of this work. A peer review file is available.